Monthly Notices
of the
ROYAL ASTRONOMICAL SOCIETY

MNRAS **484,** 950–963 (2019)
Advance Access publication 2019 January 5

doi:10.1093/mnras/stz033

He-accreting WD: nucleosynthesis in the extreme binary system (1.02 + 0.30) $M_\odot$

Luciano Piersanti [1,2]★ Lev R. Yungelson,[3] Sergio Cristallo[1,2] and Amedeo Tornambé[4]

[1]*INAF - Osservatorio Astronomico d'Abruzzo, via Mentore Maggini, snc, I-64100 Teramo, Italy*
[2]*INFN - Sezione di Perugia, Via A. Pascoli snc, I-06123 Perugia, Italy*
[3]*Institute of Astronomy of the Russian Academy of Sciences, 48 Pyatnitskaya Str, 119017 Moscow, Russia*
[4]*INAF-Osservatorio Astronomico di Roma, via Frascati, 33, I-00040 Monte Porzio Catone, Italy*

Accepted 2018 December 28. Received 2018 November 27; in original form 2018 October 9

ABSTRACT

We investigate the evolutionary properties of AM CVn stars with massive white dwarf (WD) donors and accretors. As a representative of them we consider a binary initially composed by a 0.30 $M_\odot$ He WD and a 1.02 $M_\odot$ CO WD. We evaluate the time-dependent mass transfer rate from the donor and compute the evolution of the accretor, accounting for the effects of mass exchange on the evolution of orbital parameters. We model the thermal response of the accreting CO WD with the FUNS evolutionary code coupled to a full nuclear network, from H to Bi, including more than 700 isotopes linked by about 1000 nuclear processes. We find that accretors in these systems evolve through the stages of steady He-burning and mild and strong He-flashes and become at the end CO WDs capped by a massive ($\sim$0.1 $M_\odot$) He-rich buffer. During He-flashes (both mild and strong) the temperature in the He-shell increases above 3×10^8 K, so that the ^{22}Ne$(\alpha, n)^{25}$Mg reaction becomes efficient and *n*-rich isotopes can be produced. During the Roche lobe overflow episodes triggered by strong non-dynamical He-flashes matter enriched in α-elements and *n*-rich isotopes is ejected, polluting the interstellar medium. Our results strongly suggest that massive AM CVn systems with WD donors do not experience a final very strong dynamical He-flash driving an explosive event like SN .Ia. Though the ejected matter is highly enriched in heavy isotopes, the relative contribution of massive AM CVn systems to the Galactic chemical evolution is, most probably, negligible due to their expected paucity.

Key words: accretion – nucleosynthesis – binaries: general – supernovae: general.

1 INTRODUCTION

This paper continues a series of studies of helium accretion on to carbon–oxygen white dwarfs (Piersanti, Tornambé & Yungelson 2014; Piersanti, Yungelson & Tornambé 2015, henceforth, Papers I and II, respectively). In particular, in Paper II we considered time-dependent accretion in modelling ultracompact cataclysmic variables of AM CVn type with helium white dwarf (WD) donors and CO WD accretors, also dubbed 'interacting double-degenerates' (IDD), in which the rate of mass transfer is set by angular momentum loss via emission of gravitational waves (GWs). 56 AM CVn stars were known at the time of writing (Ramsay et al. 2018). But we recall that it is suggested that, in addition to systems with WD donors, other two varieties of AM CVn stars may exist, harbouring either a low-mass helium star donor (Savonije, de Kool & van den Heuvel 1986) or a remnant of a strongly evolved main-sequence star (Tutukov et al. 1985).

A detailed description of observational properties, formation and evolution of AM CVn stars can be found, e.g. in Nelemans (2005, 2009), Solheim (2010), and Ramsay et al. (2018). We also refer the reader to Marsh, Nelemans & Steeghs (2004) for discussion of stability of mass exchange in these binaries, Paper I for investigation of regimes of He-burning at the surface of accreting CO WD in general, and to Paper II for a study of some details of unstable He-burning in AM CVn stars with variable mass-transfer rate.

Like in Paper II, the mass-transfer rate is determined by adopting the mass–radius (M–R) relation for cold degenerate stars. We use an approximation to Zapolsky & Salpeter (1969) M–R relation devised by Eggleton and published in Verbunt & Rappaport (1988). The usage of this approximation may be justified by the following circumstances. Typical delay between formation of detached He + CO WD pairs and semidetached AM CVn stars is $\sim$ Gyr (Tutukov & Yungelson 1996). On the other hand, e.g. Panei et al. (2007) have

★ E-mail: luciano.piersanti@inaf.it

shown that the radii of low-mass helium WD remnants of mass-losing stars reach asymptotical values close to those given by M–R relation of Zapolsky & Salpeter in the similar time-scale. As well, mass-transfer rates based on the latter M–R relation, excellently agree with those based on M–R relation for finite, but low-entropy WDs suggested by Bildsten et al. (2006).[1]

We remind also that, as found first by Nomoto (1982) and, most lately, e.g. in our Paper I and by Brooks et al. (2015) and Wu et al. (2017), He-burning may occur in the following regimes (in the order of increasing accretion rate $\dot{M}_{accr}$):

(i) Detonation: thermonuclear burning is initiated in degenerate layer close to CO/He interface and, if heating time-scale by nuclear reactions is shorter than dynamical time-scale of the He-burning layer, an explosion may be triggered.

(ii) Strong flashes (SF): nuclear burning starts in degenerate matter, heating time-scale does not become shorter than dynamical time-scale, but released energy is sufficient for ejection of a part or even entire accumulated He-layer, depending on the mass of accretor and $\dot{M}_{accr}$.

(iii) Mild flashes (MF): thermonuclear burning occurs in non-degenerate matter, energy release is not sufficient for ejection of matter.

(iv) Steady-state (SS) burning: WD burns accreted He into CO mixture at a rate which is slightly lower than $\dot{M}_{accr}$.

(v) RG regime: accretion rate $\dot{M}_{accr}$ is higher than accretor may burn in SS regime and excess of the matter forms an extended (red-giant-like) envelope around the WD or the envelope overflows Roche lobe of the WD.

In Paper II we studied evolution of binaries with initial accretor + donor mass combinations (0.6 + 0.17) $M_\odot$, (0.92 + 0.15) $M_\odot$, (1.02 + 0.2) $M_\odot$, which were suggested by population synthesis model of Nelemans et al. (2001). In AM CVn binaries with WD donors, $\dot{M}_{accr}$ decreases with time and, for the systems studied in Paper II, He-burning proceeded through SS-, MF-, SF regimes, but never became dynamic, as hypothesized by Bildsten et al. (2007) for the 'last' flash, occurring at the lowest $\dot{M}_{accr}$. In both Paper II and this work we neglected the effects of dynamical friction in the expanded envelope after the Roche lobe overflow (RLOF) triggered by He-flashes and we assumed that the mass transfer remains dynamically stable. At variance, Shen (2015) suggested that such an occurrence leads inevitably to the merging of the two degenerate components.

The most massive system studied in Paper II had initial masses of components 1.02 and 0.2 $M_\odot$, well inside the region where, under assumption of short time-scale of tidal synchronization in the binary, stable mass transfer at a rate below the Eddington one is possible (Marsh et al. 2004). The system we study here – (1.02 + 0.3) $M_\odot$, *aka* S102 + 030 – is just at the border of stable/unstable mass transfer. Binary population synthesis model for AM CVn stars (Nelemans et al. 2001) shows that the systems with such combinations of components masses may form, though, we clearly recognize that the results of population synthesis for any class of objects depend on specific set of accepted parameters, especially, as in the case of AM CVn stars, on the assumptions on common envelope evolution.

Like in less massive S102 + 020 system, WD in S102 + 030 experiences He-burning in SS-, MF-, and SF regimes listed above. Due to the larger mass of the accretor, during the evolution in the SF burning regime, the S102 + 030 system experiences He-flashes so strong that the temperature in the He-burning shell exceeds 3×10^8 K. In this case, α-captures on ^{22}Ne become efficient, leading to the release of neutrons via $^{22}Ne(\alpha, n)^{25}Mg$ reactions. We recall that the ^{22}Ne abundance in the He-rich layer is mainly determined by successive α-captures by ^{14}N present in the accreted matter. The latter is resulting from the conversion of the initial CNO group elements into ^{14}N via H-burning in the He WD progenitor. This implies that in the He WD which descends from the primary component of a binary system with solar chemical composition (see Papers I and II), abundance of ^{22}Ne is as large as 2.08×10^{-2} by mass fraction.[2] Neutrons delivered by the $^{22}Ne(\alpha, n)^{25}Mg$ reaction are captured by heavy elements, releasing, on average, Q∼5 MeV per each reaction, which is comparable to the energy contribution coming from 3α-reaction (Q = 7.275 MeV) and α-capture on the ^{12}C (Q = 7.162 MeV). Moreover, *n*-captures could trigger a peculiar nucleosynthesis both via *i*-process and weak *s*-process (see Section 2).

The paper is organized as follows: in Section 2, we describe the possible nucleosynthesis path in hydrogen-deficient matter under physical conditions encountered in massive AM CVn stars and we individuate the correct nuclear network to account for both the energy contribution and the chemical evolution triggered by the $^{22}Ne(\alpha, n)^{25}Mg$ reaction. In Section 3, we briefly consider the initiation of mass transfer in (1.02 + 0.3) $M_\odot$ system, which differs from the one in the systems with less massive donors. In Section 4, an overview of the evolution of the (1.02 + 0.3) $M_\odot$ binary in SF-regime is presented. In Section 5, an example of nucleosynthesis during particular strong thermal pulse is considered in detail and overall nucleosynthesis path of the system is presented. Discussion and conclusions follow in Section 6.

2 NUCLEOSYNTHESIS VIA *N*-CAPTURE PROCESSES

Elements heavier than iron are mainly synthesized by the slow neutron capture process (the *s*-process) and the rapid neutron capture process (the *r*-process). Those processes, theorized 60 yr ago by Burbidge et al. (1957), are characterized by either low ($n_n \sim 10^6 \div 10^7$ cm^{-3} for the *s*-process) or very large neutron densities ($n_n > 10^{20}$ cm^{-3} for the *r*-process).

The *r*-process produces neutron-rich isotopes very far from the β-stability valley. It was originally thought to work in the high-entropy wind of core-collapse supernovae (see e.g. Farouqi et al. 2009). In recent years, magneto-rotational supernovae have been identified as potential candidates (see e.g. Nishimura et al. 2017). Last year, the *r*-process went one step ahead of the game due to the recent neutron star merger GW170817. Characteristics of its electromagnetic counterpart AT 2017gfo are consistent with the hypothesis that during the merger event *r*-process elements were synthesized and ejected into ISM (see e.g. Kasen et al. 2017, and references therein).

During the *s*-process, instead, multiple neutron captures on a single seed nucleus (mostly ^{56}Fe) rarely occur. This is due to the fact that the β-decay half-life of freshly synthesized isotopes is shorter than the typical neutron capture time-scale. Thus, the *s*-process mainly develops along the β-stability valley. Its products

[1]Note, in the analysis of stability of mass transfer in AM CVn stars by Marsh et al. (2004), M–R relation published by Verbunt & Rappaport (1988) was used.

[2]Hereafter we address the 'mass fraction abundance' of a given isotope as 'abundance'.

are commonly subdivided into a *main* component and a *weak* component. The first is synthesized in the interiors of asymptotic giant branch (AGB) stars (Gallino et al. 1998; Straniero, Gallino & Cristallo 2006; Cristallo et al. 2015), while the latter is mainly produced during the core-He burning and shell-C burning phases of massive stars (Prantzos, Hashimoto & Nomoto 1990; Chieffi & Limongi 2013). The main neutron source in AGB stars is the $^{13}C(\alpha,n)^{16}O$ reaction, while the $^{22}Ne(\alpha,n)^{25}Mg$ reaction dominates in massive stars. Due to its rather low neutron densities ($n_n \approx 10^6$ cm^{-3}), the *weak s*-process cannot overcome the barrier opposed by nuclei with neutron magic number $N = 50$: ^{88}Sr, ^{89}Y, and ^{90}Zr. Thus, its major products are elements between the iron peak and the first *s*-process peak.

In recent years, an *intermediate* neutron capture process (the so-called *i*-process), first described by Cowan & Rose (1977), attracted a large interest with a series of recent dedicated articles (and references therein Denissenkov et al. 2017; Côté et al. 2018). This peculiar process mainly occurs when protons are mixed in a hot convective environment, producing neutron densities as large as $n_n \approx (10^{14} \div 10^{16})$ cm^{-3}. In the models published so far (proton ingestion in low-mass low-metallicity AGB stars, very late thermal pulses or born-again AGBs, WDs rapidly accreting hydrogen etc.), neutrons are released by $^{13}C + \alpha$ reactions, considering the large amount of ^{13}C synthesized via proton captures on the abundant ^{12}C.

As already recalled in the introductory section, in the S102 + 030 system a large amount of ^{22}Ne is available and, as it is shown below, at least during the SF accretion regime, the temperature at the He-burning shell attains and exceeds 3×10^8 K, so that weak *s*-process nucleosynthesis can occur. Moreover, as during the He-flashes episodes the temperature becomes $\gtrsim 5 \times 10^8$ K, the neutron densities become very large, typical for the *i*-process nucleosynthesis. It is worth recalling that during the SF regime the accretor undergoes recurrent RLOF episodes, so that at a certain moment, when the He-flash is strong enough, the ejected matter becomes enriched in *n*-rich isotopes.

In order to properly describe the nucleosynthesis and the energy generation in the flashing S102 + 030 system we adopted in our computation a large nuclear network, including isotopes from hydrogen to the heaviest stable ones (^{209}Pb and ^{210}Bi). The original network was introduced by Straniero et al. (2006) to follow standard *s*-process; successively, it was extended by Cristallo et al. (2011) to account for very large neutron exposure. In this work, the nuclear network includes about 700 isotopes linked by 1000 nuclear processes, including α-, *p*-, *n*-captures as well as β-decays (see also Cristallo et al. 2016).

3 THE ONSET OF NUCLEAR BURNING

Initial parameters of the accreting CO WD chosen in this study are $M_{CO,i} = 1.02047$ M$_\odot$, central temperature and density $T_C = 1.71 \times 10^7$ K and $\rho_C = 4.082 \times 10^7$ g cm^{-3}, respectively, $\log(L/L_\odot) = -2.03$, and $\log(T_{eff}) = 4.31$. At the onset of the mass transfer process the orbital separation of components is $a = 0.0614 R_\odot$, corresponding to the orbital period $\simeq 2.21$ min. We assume, as in Paper II, that the expansion of the accreting WD is limited by its Roche lobe and excess of the matter is expelled from the system with the specific angular momentum of the accretor.

Evolution of the S102 + 030 system at the beginning of the mass transfer process is quite similar to that of the S102 + 020 (see Paper II), though, there exist some important differences. Fig. 1 shows the evolution of the S102 + 030 system during this early phase of mass transfer. When, due to GW emission,

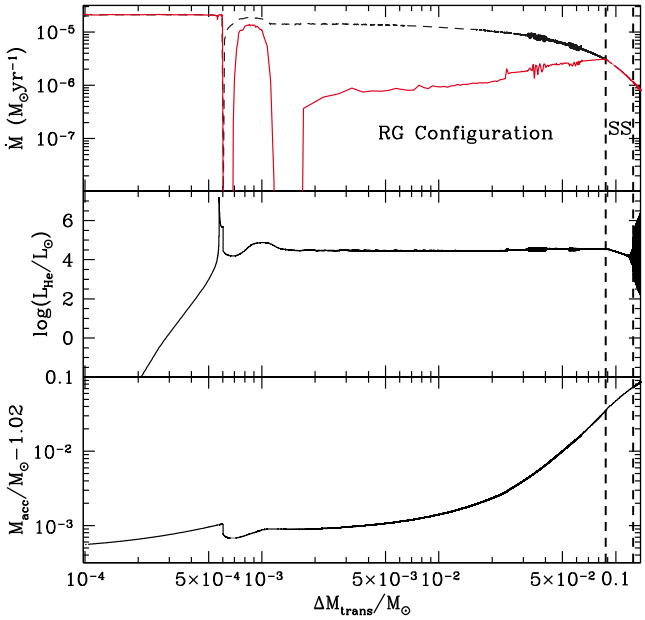

Figure 1. Evolution of the S102 + 030 system during the first two He-flash episodes and during the 'RG Configuration' regime. Upper panel: mass transfer rate from the donor (dashed line) and effective mass deposition rate on to the accretor (solid line).

He WD fills its Roche lobe, mass transfer begins at a very high rate ($\dot{M}_{tran} \sim 2.12 \times 10^{-5}$ M$_\odot$ yr^{-1}), close to the Eddington limit, while in model S102 + 020 it was an order of magnitude lower ($\dot{M}_{tran} \sim 2.2 \times 10^{-6}$ M$_\odot$ yr^{-1}).

As a consequence, in the model S102 + 030 thermal energy at the surface of the accreting WD is delivered at a definitively larger rate, so that the first flash occurs after 5.6×10^{-4} M$_\odot$ of He-rich matter has been accreted, while in the model S102 + 020 He-rich buffer piled up before the first flash was substantially more massive ($\sim 2.03 \times 10^{-3}$ M$_\odot$). At the onset of the He-flash, matter at the base of the He-rich buffer is less degenerate in model S102 + 030 than in model S102 + 020, so that the flash itself is less strong. This is evident when considering the maximum luminosity during the He-flash L_{He}^{max}, which is equal to 1.43×10^7 L$_\odot$ and 3.74×10^9 L$_\odot$ in models S102 + 030 and S102 + 020, respectively.

Energy release by the first thermonuclear flash results in the expansion of the accreting WD which fills its Roche lobe. Formation of the contact system leads to mass and angular momentum loss from the system. As a consequence the orbital separation increases and the donor detaches from its Roche lobe (Figs 1 and 2). In binaries of lower mass (see Paper II), the He WD donor fills again its Roche lobe after the He-flash died-down as, due to the GW emission, the binary system shrinks. In the more massive system under consideration, mass transfer from the donor resumes very soon, when He-burning is still providing the entire surface luminosity (see Table 1). Such an occurrence is related to the fact that the amount of matter lost during the RLOF episode is quite small so that the system does not expand too much. As a consequence, when $\simeq$ 51 per cent of the previously accreted matter has been lost from the system (i.e. $\Delta M_{lost} \simeq 3 \times 10^{-4}$ M$_\odot$), GW emission determines the onset of a new mass transfer episode. At that epoch, the accretor is still filling its Roche lobe, so that all the matter transferred from the donor is lost from the system and also the most external layers of the CO WD are eroded (see upper and lower panels in Fig. 2). When He-burning efficiency definitively decreases, the

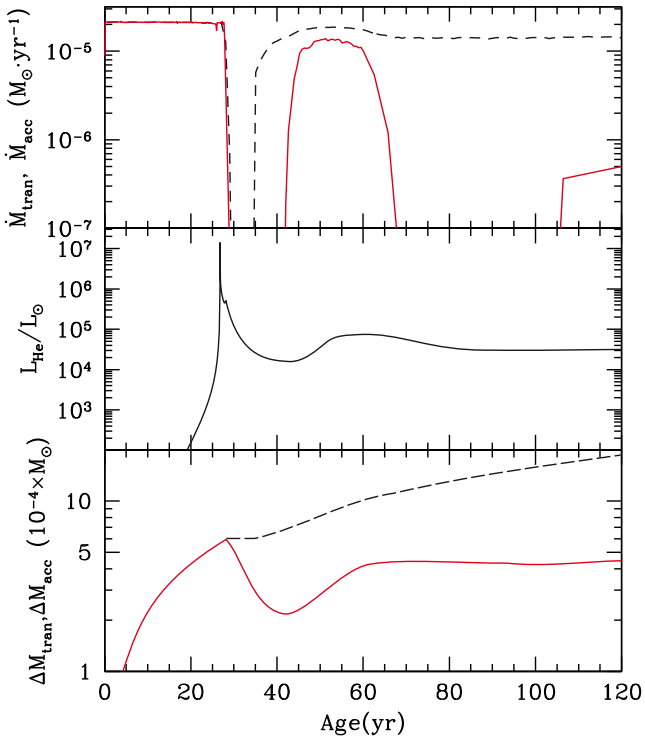

Figure 2. Evolution of the S102 + 030 system during the first two He-flash episodes. The same quantities as in Fig. 1 are reported, but as a function of the time elapsed from the onset of mass transfer. In the lower panel the amounts of matter transferred from the donor $\Delta M_{\rm tran}$ (dashed line) and the matter deposited on to the accreting CO WD $\Delta M_{\rm acc}$ (solid line) are plotted.

accretor can start to receive mass again. However, as $\dot{M}$ from the donor is still very high ($\dot{M}_{\rm tran} \simeq 2.09 \times 10^{-5}$ M$_\odot$ yr^{-1}), the further evolution of the S102 + 030 system occurs in the RG configuration accretion regime. After accreting additional 10^{-4} M$_\odot$ the CO WD experiences a second very mild He-flash ($L_{\rm He}^{\rm max} \sim 3L_{\rm star}$), which represents an additional engine to the expansion of the He-rich layers. As a matter of fact, in the following evolution the whole mass transferred from the donor as well as part of the external layers of the accretor are lost by the system. At variance with the first He-flash episode, the system does not detach at all so that mass is transferred from the donor continuously. When the He-burning luminosity decreases to $\log(L_{\rm He}/{\rm L}_\odot) = 4.466$, the accretor starts to increase its mass again.

As matter is transferred from the donor, the mass transfer rate decreases, but remains for some time in the range (10^{-5}–10^{-6}) M$_\odot$ yr^{-1}. However, accreting WD can burn steady only less than *several* $\times 10^{-6}$ M$_\odot$ yr^{-1}; excess of the matter should form an extended red-giant-like (RG) envelope (Paper I). This means that the compact system is losing mass, being immersed into this envelope. We assume that spiral-in does not happen, since excess of the matter is minuscule, only several hundredth of M$_\odot$, and the matter is lost from the system. Really, during the RG configuration regime the transferred mass is equal to 8.684×10^{-2} M$_\odot$, while the mass effectively accreted is equal to 3.415×10^{-2} M$_\odot$; hence, the average retention efficiency is 39.3 per cent.

Next, the system enters steady-burning regime, when the matter transferred to the accretor is partially burned at $\dot{M} \sim 10^{-6}$ M$_\odot$ yr^{-1} and partially accumulated in the non-expanding envelope.

We neglected above the effects of tidal heating and possible tidal Novae occurring when systems are close to contact (e.g. Iben, Tutukov & Fedorova 1998; Fuller & Lai 2012), since hydrogen-rich surface layers of massive post-common-envelope CO WD, which may be involved, are expected to have very low mass, $\simeq 3 \times 10^{-5}$ M$_\odot$ (Lauffer, Romero & Kepler 2018).

4 THE PHYSICAL EVOLUTION OF S102 + 030 SYSTEM

The evolution during the SS-, MF-, and SF regimes does not deserve any particular analysis as compared to model S102 + 020 in Paper II: the mass transfer rate from the donor decreases, the mass ratio (mass of the primary over mass of the secondary) increases, and the separation of components increases.

In Fig. 3, we plotted the main physical characteristics of the He-burning shell. Accreting CO WD enters the MF regime when its mass is 1.0927 M$_\odot$ and the donor mass is 0.1751 M$_\odot$. At this epoch, the mass transfer rate is equal to $\dot{M} = 1.152 \times 10^{-6}$ M$_\odot$ yr^{-1}. By comparing $M_{\rm acc}$ and $\dot{M}$ values with those derived in Paper I, we find that the transition from the SS to the MF regime occurs at a slightly lower $\dot{M}$ for a fixed $M_{\rm acc}$, due to the gravothermal energy delivered by the compression of the C-rich layers piled up via He-burning. The onset of the SF regime occurs when $M_{\rm acc} \simeq$1.1047 M$_\odot$, and $\dot{M}_{\rm tran} = 8.14 \times 10^{-7}$ M$_\odot$ yr^{-1}. Accreting WD experiences 87 He-flashes, progressively stronger as $M_{\rm acc}$ increases and $\dot{M}_{\rm tran}$ decreases. When mass transfer resumes after the last He-flash, the mass transfer rate from the donor is $\dot{M}_{\rm tran} = 4.10 \times 10^{-8}$ M$_\odot$ yr^{-1}and the mass of the accretor is $M_{\rm acc} = 1.1312$ M$_\odot$. By extrapolating results in Paper I, if the mass transfer rate would remain equal to such a value, a dynamical He-flash should occur after $\Delta M_{\rm He} \sim 0.04$ M$_\odot$ has been accreted. But, as already observed in Paper II, in binary systems with He-WD donor $\dot{M}_{\rm tran}$ continuously decreases and, hence, $\Delta M_{\rm He}$ becomes larger and larger as $M_{\rm don}$ reduces. As a matter of fact we find that all the residual mass is transferred to the CO WD without triggering a new He-flash. Hence the final outcome of the evolution of S102 + 030 system is the formation of a massive WD, having a CO core of ∼1.1173 M$_\odot$ capped by a He-rich layer of 0.1004 M$_\odot$.

Small 'irregularities' in the curves for $T_{\rm He}$ and $\rho_{\rm He}$ between outbursts, which become visible in Fig. 3 for $M_{\rm don} \lesssim 0.13$ M$_\odot$, reflect change in the position of $\varepsilon_{3\alpha,\,\rm max}$, which depends on temperature, density, and He abundance.

As it is well known, and also displayed in Fig. 3, He-flashes become stronger as the mass transfer rate decreases. This implies that, pulse by pulse, the RLOF episode following each He-flash occurs sooner, while the He-burning shell is still delivering a huge amount of energy, driving a very rapid expansion of the accreting WD. As a consequence the mass-loss rate from the accretor becomes progressively larger; in particular we find that the RLOF episode triggered by the last He-flash lasts for 21.92 yr and that $\simeq 6.9 \times 10^{-3}$ M$_\odot$ is lost, the mass-loss rate exceeding 1 M$_\odot$ yr^{-1}at the beginning of the flash.

For each He-flash occurring in the SF accretion regime we derive the retention efficiency along the cycle η, defined as in Paper I:

$$\eta = 1 - \frac{\Delta M_{\rm L}}{\Delta M_{\rm tr}^1 + \Delta M_{\rm tr}^2}, \qquad (1)$$

where ΔM$_{\rm L}$ is the mass lost during the RLOF, while ΔM$_{\rm tr}^1$ and ΔM$_{\rm tr}^2$ are the mass accreted on to the WD before and after the RLOF episode, respectively. The obtained values are reported in Fig. 4 as a function of the accretor total mass at the bluest point along each loop in the HR diagram.

Table 1. Selected physical properties of the system S102 + 030 during the first He-flash episode. The various epochs are: A – onset of the flash-driven convective shell; B – ignition of He-burning; C – maximum luminosity of the He-burning shell; D – beginning of the RLOF episode; E – disappearance of flash-driven convective shell; F – resumption of the mass transfer from the donor; G – resumption of effective mass deposition on to accretor. For each epoch we list the time elapsed between two successive epochs Δt in yr, the total mass of the accretor M_{acc} and of the donor M_{don} in $M_\odot$, the separation of components a in 10^{-2} $R_\odot$, the effective temperature T_{eff} and luminosity $L/L_\odot$, mass coordinate of the He-burning shell M_{He} in $M_\odot$, the density ρ_{He} in 10^3g cm^{-3}, the temperature T_{He} in 10^8 K, and luminosity $L_{He}/L_\odot$ of the He-burning shell. The Δt for epoch A refers to the time from RLOF by donor WD to the onset of the flash-driven convective shell in accreting WD.

	A	B	C	D	E	F	G
Δt (yr)	26.632	0.071	0.053	1.177	6.085	0.686	7.120
$M_{acc}/M_\odot$	1.021028	1.021030	1.021031	1.021056	1.020784	1.020760	1.020678
$M_{don}/M_\odot$	0.299438	0.299437	0.299436	0.299411	0.299406	0.299406	0.299329
a (in 10^{-2} $R_\odot$)	6.1519	6.1519	6.1519	6.1523	6.1520	6.1519	6.1528
log (T_{eff})	5.746	5.745	5.698	5.675	5.681	5.684	5.703
log($L/L_\odot$)	3.916	3.914	3.835	4.608	4.632	4.645	4.713
$M_{He}/M_\odot$	1.02061	1.02057	1.02051	1.02029	1.02017	1.02007	1.02048
ρ_{He}	8.358	7.700	3.888	5.210	4.896	7.226	1.154
T_{He}	1.979	2.288	3.350	2.934	3.007	2.890	2.340
log($L_{He}/L_\odot$)	5.026	5.918	7.154	5.650	4.501	4.440	4.196

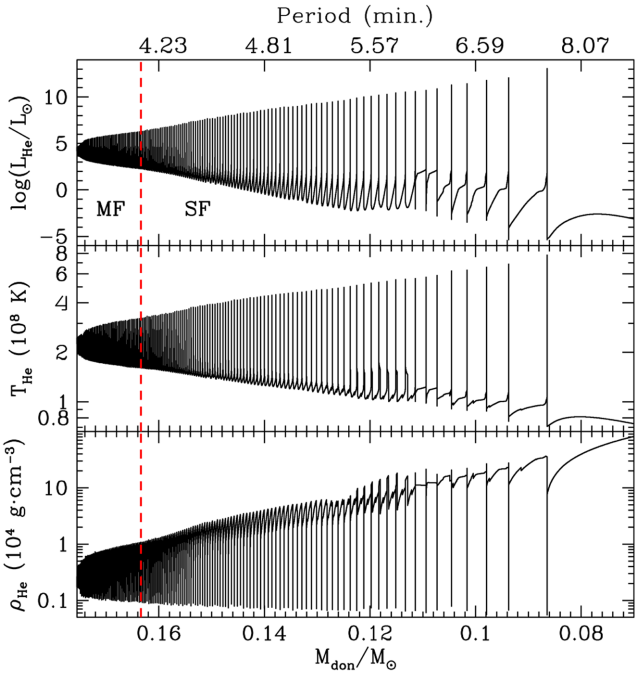

Figure 3. Physical properties of He-burning shell of the accretor of the system S102 + 030 during the MF- and SF regimes. From bottom to top: density, temperature, the energy delivered per unit time via He-burning. The red heavy dashed lines mark the transition from one burning regime to the other. Lower x-axis: mass of the donor in solar masses; Upper x-axis: orbital period in minutes.

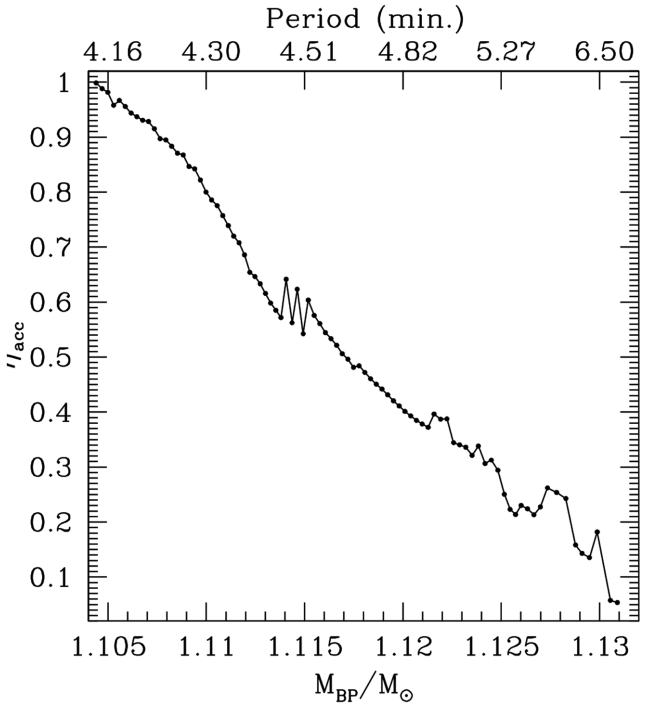

Figure 4. Retention efficiency during the SF regime as a function of the accretor mass at the bluest point along the loop in the HR diagram (lower x-axis) and of the orbital period (upper x-axis).

As discussed in Paper II, the value of η reduces on average, as $\dot{M}_{tran}$ decreases, even if the curve exhibits an irregular behaviour. Once again, as we already suggested in the past (see Paper II), such an occurrence has to be ascribed to the interplay of (1) decreasing mass transfer rate, (2) 'dead-time' span, between the end of RLOF and the re-onset of mass transfer, and (3) gravothermal energy delivered by the contraction of the freshly synthesized CO-rich layers below the actual He-mantle.

A further inspection of Fig. 3 discloses that the temperature in the He-burning shell exceeds 3×10^8 K already during the MF accretion regime, so that the ^{22}Ne(α, n)^{25}Mg reaction becomes active. This demonstrates that in the computation of the evolution of S102 + 030 system a nuclear network involving all the relevant n-capture processes is needed to correctly evaluate both the nucleosynthesis and the delivered nuclear energy. To elucidate the importance of n-captures in the physical evolution of the S102 + 030 system we repeat the computation by neglecting all nuclear processes involving neutrons. In Fig. 5, we report the evolution of the accretor total mass as a function of the donor total mass for both cases. As it can be noticed, when the contribution from n-captures is accounted for (lower solid black curve), the accreting WD enters the SF regime

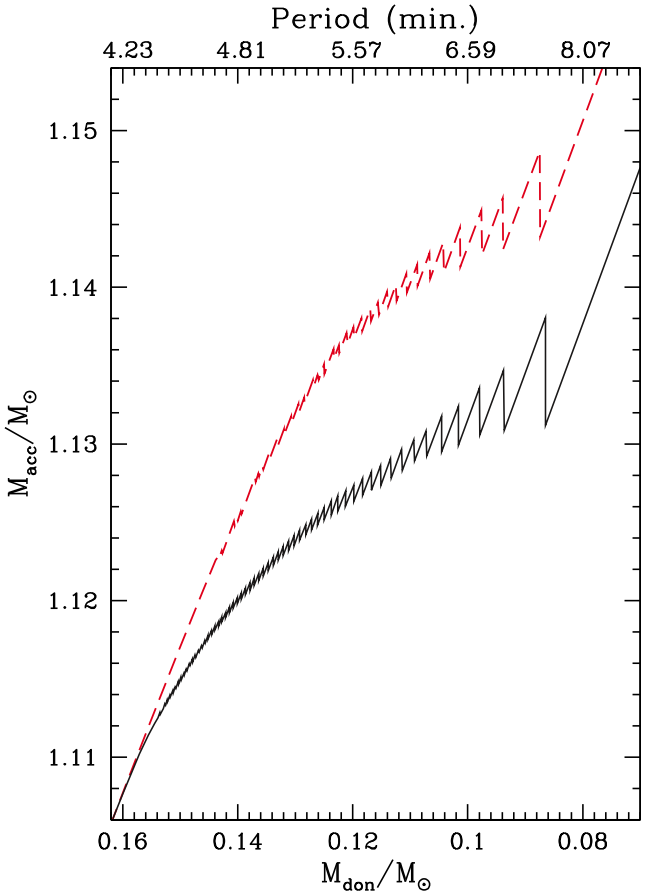

Figure 5. Solid line – mass of the accretor as a function of the donor mass during the SF accretion regime. Dotted red line – the same quantity, but for a model computed neglecting the nucleosynthetic and energetic contribution coming from *n*-captures. Upper *x*-axis reports the orbital period (in minutes).

earlier and the retention efficiency is lower for the same mass lost by the donor. Thus, when the contribution from *n*-captures is neglected (dotted red curve), a more massive WD is formed even if the final outcome of the accretion process remains unchanged.

Particular evolutionary stages considered above last for $\Delta T_{\rm RG} = 1.39 \times 10^4$ yr, $\Delta T_{\rm SS} = 2.39 \times 10^4$ yr, $\Delta T_{\rm MF} = 8.83 \times 10^3$ yr, $\Delta T_{\rm SF} = 5.65 \times 10^5$ yr. For the latter phase we refer to the time from the onset of the first strong He-flash (i.e. the epoch corresponding to the bluest point along the loop in the HR diagram of the first strong He-flash) to the resumption of mass transfer after the last (87th) strong He-flash.

5 THE CHEMICAL PROPERTIES OF THE EJECTED MATTER

We remind that, as already mentioned in the previous section, the temperature at the base of the He-burning shell exceeds 3×10^8 K already during the MF phase. This implies that the ^{22}Ne(α, n)^{25}Mg reaction is ignited very soon in the evolution of the system, so that during the He-flash neutrons are produced activating the corresponding nucleosynthesis of *n*-rich isotopes. However, we do not analyse this nucleosynthesis because during the MF regime no matter is lost from the accreting WD, so that there is no way to observe the imprint of these episodes. In fact, as demonstrated above, the S102 + 030 system does not produce any explosive event destroying the accreting WD.

5.1 Heavy elements production in binary systems: a case study

In order to illustrate how the nucleosynthesis proceeds during the SF regime, we focus our attention on the 38th He-flash episode, when the mass of the accretor at the re-onset of mass transfer from the donor is $\sim$1.1149 M$_\odot$. We choose this episode because the physical properties during the He-flash and the subsequent RLOF episode are such that the efficiency of *n*-capture nucleosynthesis is at a maximum. In particular, the temperature in the He-rich buffer remains larger than the critical value for efficient neutrons production via ^{22}Ne(α, n)^{25}Mg reaction for almost the entire time of the flash and of the subsequent RLOF episode. Moreover the convective shell triggered by the He-flash lasts long enough to guarantee a large neutron exposure (see below).

In the left-hand panel of Fig. 6[3] we report the evolution of the accreting WD in the HR diagram; some relevant epochs are marked by heavy dots and numbers. The temperature profiles in the outermost zone of the CO-core and in the He-rich mantle for each of these models are plotted in the right-hand panel of Fig. 6, while the abundances of some key isotopes are reported in Fig. 7. We select ^{4}He as a tracer of He-burning, ^{14}N and ^{22}Ne as tracers of ^{22}Ne(α, n)^{25}Mg reaction efficiency, ^{25}Mg as a tracer of ^{22}Ne destruction and neutrons production, ^{24}Mg as a tracer of the α-capture reactions, ^{88}Sr, ^{75}As, and ^{139}La as tracers of *n*-capture nucleosynthesis. In Table 2, we list some physical properties of the accretor at the epochs marked in Figs 6 and 7.

Point 1 in Fig. 6 corresponds to the resumption of mass transfer from the donor. At that epoch the He-rich buffer is still hot, due to the energy injected during the previous He-flash episode, even if thermal energy is flowing inwards, as clearly demonstrated by the broad shape of the corresponding temperature profile in the right-hand panel of Fig. 6. As shown in panel 1 of Fig. 7, the surface abundances of ^{4}He and ^{12}C are 0.835 and 0.133, respectively, clearly demonstrating the effects of the previous He-flash episodes. Due to the inward thermal diffusion, He-rich buffer piled up via mass deposition rapidly becomes isothermal. After $\Delta t_{12} \approx 873$ yr, due to the continuous mass deposition, the He-shell, located at $\sim$1.1148 M$_\odot$, heats up to 1.608×10^8 K, while the density increases up to 2.428×10^4 g cm^{-3}(see also the flat portion in the temperature profile labelled 2 in the range $x = ({\rm M/M_\odot} - 1.1) \times 10^2 = 1.48$–$1.49$ in the right-hand panel of Fig. 6). At the epoch 2, He-burning already delivers $L_{\rm He} \sim 1.23 \times 10^3$ L$_\odot$, a factor 2 larger than the surface luminosity of the accreting WD. The increase of temperature in the He-rich buffer determines also the burning of ^{14}N into ^{22}Ne, as it is seen by comparing the lowest parts of the lines for this isotope in panels 1 and 2 of Fig. 7 (at $x \sim 1.49$). After $\Delta t_{23} = 5.93$ yr the temperature in the He-shell increases to 1.643×10^8 K and He-burning delivers $L_{\rm He} \simeq 5.61 \times 10^3L_\odot$. At this epoch, He-burning is fully ignited, even if no substantial nucleosynthesis has occurred so far.[4] In the following evolution, from point 3 to point 4 in the left-hand panel of Fig. 6, lasting for $\Delta t_{34} = 240$ d, the thermonuclear runaway develops, thus triggering the onset of a convective shell which grows in mass outwards (see the jumps in the ^{22}Ne, ^{25}Mg,

[3]Colour version of Figs 6–12 are available in the online version.
[4]Let us remark that we define the He-burning ignition as the epoch when the energy delivered via 3α-reactions per unit time exceeds by a factor 100 the surface luminosity of the accreting WD.

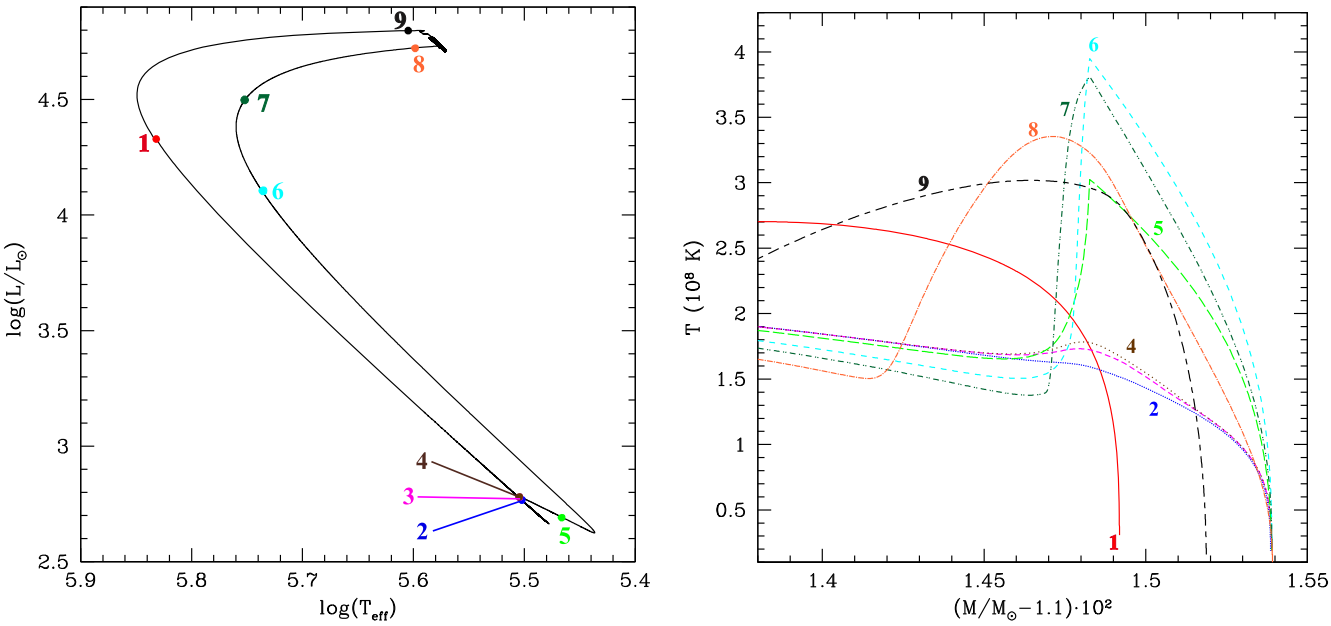

Figure 6. Left-hand panel: evolution of the accretor in the HR diagram during the 38th He-flash. Some relevant epochs are marked by filled dots and numbers. Right-hand panel: temperature profile as a function of the mass coordinate for the selected models in the left-hand panel, as labelled inside the plot.

^{88}Sr, and ^{75}As profiles in panel 4 of Fig. 7). Note that, as it is well known, during the rapid increase of the energy locally delivered, the He-burning shell and, as a consequence, the inner border of the convective shell driven by the He-flash itself, move inwards in mass (see Paper II). This determines the enrichment of the He-rich zone with isotopes synthesized during the previous He-flash episode (see the increase of ^{22}Ne, ^{25}Mg, ^{88}Sr, and ^{75}As abundances in the range $x \sim 1.49$–1.51).

In the next $\Delta t_{45} = 314$ d, the temperature in the He-burning shell has reached 3.025×10^8 K, and the convective shell has practically attained its maximum extension (note the inward penetration of the inner border of the convective shell by comparing panels 4 and 5 in Fig. 7). During this time span, ^{14}N has been efficiently converted into ^{22}Ne in the entire convective shell. In the following evolution, from 5 to 6, lasting for 7.5 d, $T_{\rm He\text{-}shell}$ continues to increase up to its maximum value over the pulse, equal to 3.948×10^8 K.

As the temperature at the He-shell exceeds the threshold value for the activation of the ^{22}Ne$(\alpha, n)^{25}$Mg reaction, ^{22}Ne is efficiently destroyed there (see the local minimum in the ^{22}Ne profile in panel 6 of Fig. 7), determining the onset of neutron-isotopes nucleosynthesis. Isotope ^{25}Mg produced at the base of the He-rich envelope as well as the products of *n*-capture processes (represented by ^{88}Sr, ^{75}As, and ^{139}La in Fig. 7) is diluted over the whole convective region. When the accreting CO WD starts to expand noticeably (at point 6 in the left-hand panel of Fig. 6), thermal energy starts to be transferred inwards, so that, after $\Delta t_{67} \sim 34.9$ d, the temperature in the He-burning shell decreases to 3.812×10^8 K. The right-hand panel in Fig. 6 also shows that below the He-burning shell the temperature has increased above the threshold value for the activation of ^{22}Ne$(\alpha, n)^{25}$Mg reaction so that the ^{22}Ne abundance decreases also in the radiative zone between $x = 1.475$ and $x = 1.48$ (see panel 7 in Fig. 7). This process continues also during the next $\Delta t_{78} \sim 3.565$ yr up to the onset of the RLOF by the CO WD at epoch 8. It is worth noticing that at the epoch 8, ^{22}Ne has been efficiently consumed up to $x \sim 1.46$. The RLOF episode lasts for $\Delta t_{89} \sim 8.627$ yr. During RLOF, about 2.17×10^{-4} M$_\odot$ are lost, corresponding to ~ 45.7 per cent of the He-rich matter transferred from the donor.

As it is clearly shown by comparison of panel 2, external part of panel 8 and panel 9 in Fig. 7, ejected matter is enriched, compared to ISM, by ^{4}He itself and by the He-burning products, mainly ^{12}C, ^{16}O, ^{20}Ne, ^{24}Mg, by ^{25}Mg – the tracer of ^{22}Ne$(\alpha, n)^{25}$Mg reaction, as well as by *n*-rich isotopes, traced by ^{88}Sr, ^{75}As, and ^{139}La. Accreted ^{14}N is completely reprocessed.

5.2 The overall nucleosynthesis path

In order to understand and properly describe the nucleosynthesis processes occurring in the S102 + 030 system, it is useful to preliminary analyse the variation of neutron density during recurrent strong He-flashes. Such a quantity n_n is defined as

$$n_n = \frac{X(n)}{A(n)} \cdot \rho \cdot N_{\rm A}, \qquad (2)$$

where ρ is the local density, $N_{\rm A}$ is the Avogadro's number, $X(n)$, $A(n)$ the abundance and the mass number of neutrons, respectively. A sizable *n*-capture nucleosynthesis can occur only if $n_n > 10^9$ cm^{-3}. In Fig. 8, we report the time evolution of the maximum neutron density $n_n^{\rm max}$ for the 4th, 38th, 67th, 76th, and 87th He-flash episodes. Usually these quantities refer to the He-burning shell or to the layer above it, where ^{22}Ne$(\alpha, n)^{25}$Mg reactions occur.

For each selected model, we fix the time origin at the epoch when the temperature at the He-burning shell first exceeds 3×10^8 K, corresponding to the epoch when ^{22}Ne$(\alpha, n)^{25}$Mg reactions deliver neutrons at a sizable level.

In Table 3, we report for the five selected models the mass of the accreting WD at the bluest point along the loop in the HR diagram, the maximum temperatures attained during the He-flash episode, the time span during which the maximum neutron density is larger than 10^9 cm^{-3} and the *total neutron exposure*, i.e. the time-integrated

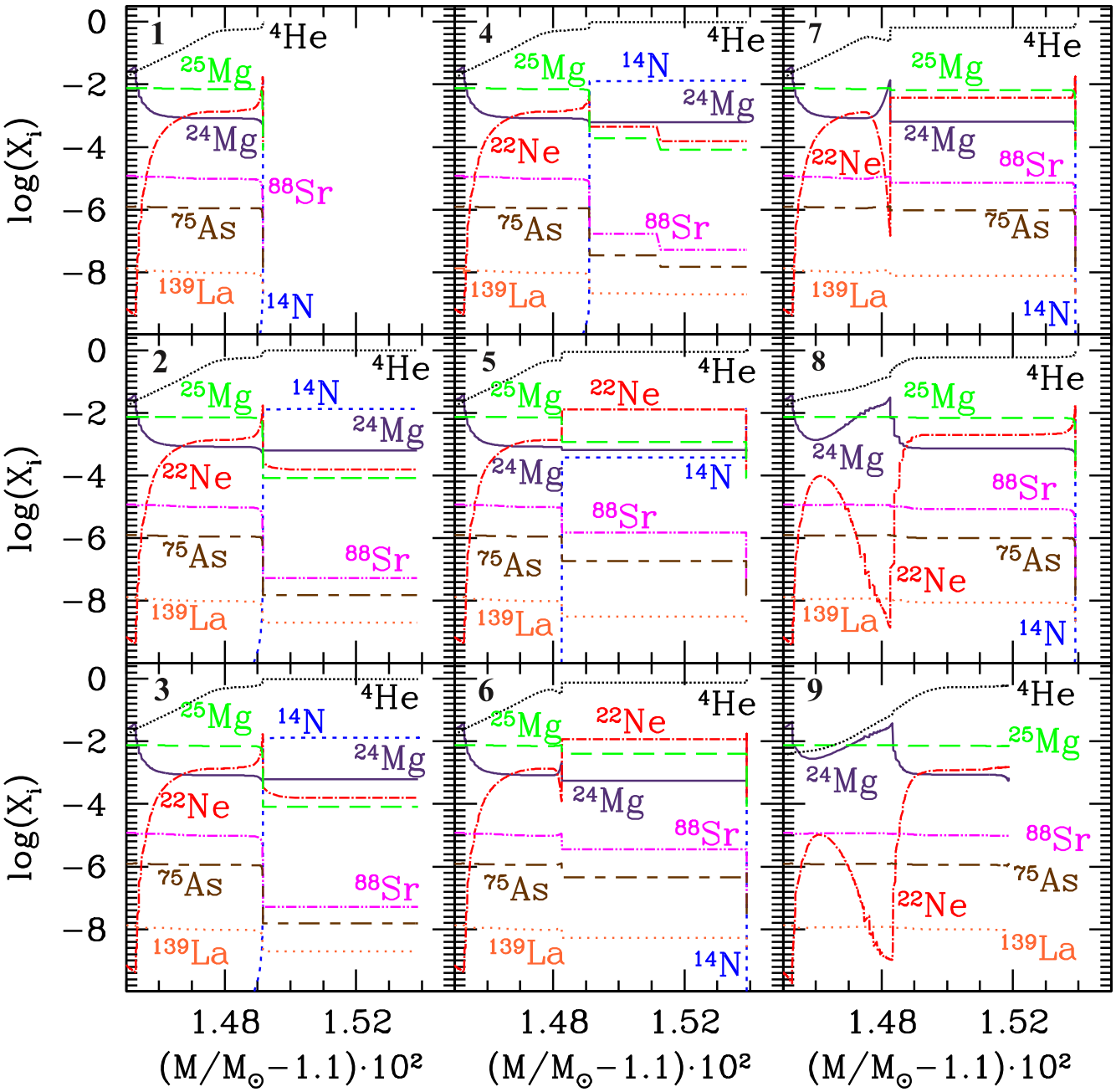

Figure 7. Abundances profile as a function of the mass coordinate of selected isotopes for the accreting CO WD at the epochs marked in the left-hand panel of Fig. 6. Fine-dotted lines: ^{4}He; short-dashed lines:^{14}N; dot–dashed lines: ^{22}Ne; solid lines: ^{24}Mg; long-dashed lines: ^{25}Mg; short–long dashed: ^{75}As; double-dotted dashed lines: ^{88}Sr; dotted lines: ^{139}La.

neutron flux, defined as

$$\delta\tau = \int_{\Delta t} n_n \cdot v_{\rm th} {\rm d}t, \tag{3}$$

where $v_{\rm th} = \sqrt{2k_{\rm B}T/m_n}$ is the average thermal velocity of neutrons (Gallino et al. 1998).

As it can be noticed, at the beginning of the SF accretion regime, when the WD mass is lower than ∼1.11 M$_\odot$, the maximum temperature attained during He-flashes is ∼3 × 10^8 K, so that $n_n^{\rm max}$ is lower than 3 × 10^{11} cm^{-3} and nucleosynthesis in the *s*-process regime can occur. As the WD mass increases, the temperature increases, attaining ∼7.6 × 10^8 K in the last episode. However, the largest values for $n_n^{\rm max}$ (above ∼10^{15} cm^{-3}), typical for the *i*-process regime are attained only in the last 11 He-flashes.

At variance, the time over which the matter is exposed to high neutron densities (hereinafter *exposure time*) decreases, as M$_{\rm WD}$ increases, (and, thus, as the evolutionary time elapses). Notwithstanding the total neutron exposure increases so that the production of heavy elements via *n*-captures should increase as the accreting WD continues to grow in mass.

In Figs 9–12 we plot the abundances of some selected isotopes in the outermost zones of the accreting WD after it has experienced RLOF triggered by the 87th (i.e. the last) He-flash, while in the third column of Table 4 we list the abundance of the same isotopes

Table 2. Selected physical properties of the system S102 + 030 during the 38th He-flash episode in the strong flashes accretion regime. The various epochs are the same displayed in Figs 6 and 7. The same quantities as in Table 1 are listed.

	1	2	3	4	5	6	7	8	9
Δt (yr)	–	873.33	5.93	0.66	0.86	0.02	0.10	3.56	8.63
$M_{acc}/M_\odot$	1.114929	1.115397	1.115400	1.115400	1.115400	1.115400	1.115400	1.115402	1.115186
$M_{don}/M_\odot$	0.149851	0.149383	0.149380	0.149380	0.149379	0.149379	0.149379	0.149377	0.149377
a (in $10^{-2}R_\odot$)	9.7453	9.7649	9.7651	9.7651	9.7651	9.7651	9.7651	9.7652	9.7662
$\log(T_{eff})$	5.832	5.502	5.505	5.505	5.466	5.736	5.752	5.598	5.605
$\log(L/L_\odot)$	4.329	2.767	2.779	2.780	2.691	4.105	4.498	4.722	4.798
$M_{He}/M_\odot$	1.11478	1.1148	1.11481	1.11481	1.11483	1.11483	1.11483	1.11488	1.11498
ρ_{He}	3.932	24.277	16.676	16.637	9.395	6.235	1.571	0.851	1.686
T_{He} (in 10^8 K)	2.057	1.608	1.643	1.687	3.025	3.948	3.812	3.153	2.820
$\log(L_{He}/L_\odot)$	3.218	3.091	3.749	3.975	7.619	9.034	6.451	4.939	4.540

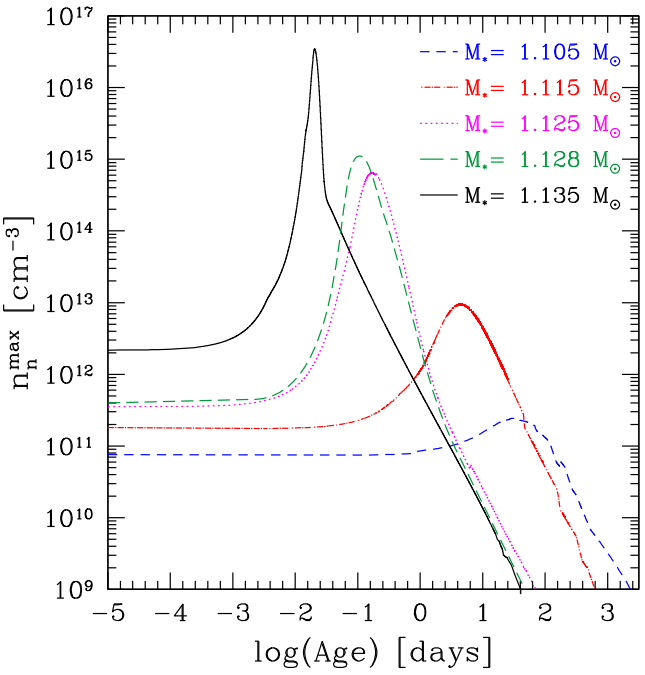

Figure 8. Temporal evolution of the maximum neutron density attained during the 4th (short dashed line), 38th (dot–dashed line), 67th (dotted line), 76th (long-dashed line), and 87th (last) strong He-flashes (solid line). For each flash, we fix the time origin at the epoch when the temperature at the He-burning shell first exceeds 3×10^8 K.

Table 3. From left to right we list the number of the strong He-flash, the value of the WD total mass (in $M_\odot$) at the bluest point along the HR loop, the maximum temperature (in 10^6 K) attained at the He-shell during the flash, the time duration of the evolutionary phase during which $n_n^{max} > 10^9$ cm^{-3} and the total neutron exposure (in mbarn^{-1}).

N.	M_{BP}	$T_{max}[10^6 K]$	Δt	$\delta\tau$ [mbarn^{-1}]
4	1.105	331	6.3 yr	0.730
38	1.115	395	1.7 yr	2.317
67	1.125	491	70.8 d	3.162
76	1.128	528	45.8 d	4.300
87	1.135	762	40.2 d	4.931

in the accreted matter (X_{acc}). The displayed layers have been piled up in the SF accretion regime so the chemical composition there traces the subsequent nucleosynthesis episodes. According to the discussion in the previous subsection, as soon as the temperature

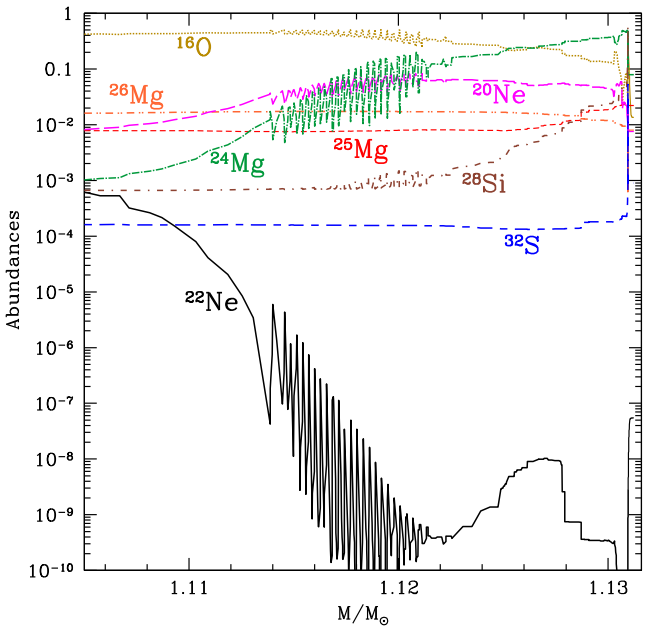

Figure 9. Abundances of selected light isotopes in the most external zone of the accreting WD, piled up during the SF accretion regime. Dotted line: ^{16}O; long-dashed line: ^{20}Ne; solid line: ^{22}Ne; dot–dashed line: ^{24}Mg; short-dashed line: ^{25}S; double-dot dashed line: ^{26}Mg; double-dash dotted line: ^{28}Si; long–short dashed line: ^{32}S.

in the He-rich buffer increases above 3×10^8 K during the flash episode, ^{22}Ne is consumed. Fig. 9 discloses that soon after entering the SF accretion regime, the temperature at the He-shell is so large that the ^{22}Ne$(\alpha, n)^{25}$Mg reaction is very efficient. This is evident when considering that ^{22}Ne abundance before the activation of this neutron source is determined mainly by the amount of ^{14}N in the accreted matter and, hence, it is as large as 2.08×10^{-2} (see Section 1). As a matter of fact, at the epoch of the 28th He-flash episode, corresponding to the WD mass $M_{BP} \simeq 1.112\ M_\odot$, the ^{22}Ne abundance decreases to X(^{22}Ne)$\simeq 2 \times 10^{-5}$. The saw-tooth behaviour observed in Fig. 9 for $1.114 < M/M_\odot < 1.121$ (corresponding to the 35th and 62th He-flash episodes) is determined by the fact that the evolutionary time-scale during the flash episode becomes shorter and shorter so that the mixing efficiency in the He-rich buffer drastically decreases. As a consequence, during the flash, when the energy delivered by nuclear burning is still driving the increase of the He-shell temperature, the transport of ^{22}Ne down into the burning zones becomes less efficient. The local

Table 4. Abundances of some selected isotopes in the matter accreted on to the CO WD (X_{acc}) and in the entire mass ejected during 87 strong He-flashes (X_{ej}).

Isotope	Z	X_{acc}	X_{ej}
^{4}He	2	0.98	4.98×10^{-1}
^{12}C	6	0.00	3.80×10^{-1}
^{14}N	7	1.31×10^{-2}	4.27×10^{-5}
^{16}O	8	0.00	1.90×10^{-2}
^{19}F	9	4.97×10^{-7}	3.16×10^{-8}
^{20}Ne	10	1.94×10^{-3}	8.36×10^{-3}
^{22}Ne	10	1.55×10^{-4}	5.09×10^{-4}
^{23}Na	11	4.16×10^{-5}	5.51×10^{-5}
^{24}Mg	12	6.24×10^{-4}	4.95×10^{-2}
^{25}Mg	12	8.23×10^{-5}	1.32×10^{-2}
^{26}Mg	12	9.42×10^{-5}	1.33×10^{-2}
^{27}Al	13	7.22×10^{-5}	2.38×10^{-4}
^{28}Si	14	8.11×10^{-4}	1.33×10^{-2}
^{31}P	15	9.74×10^{-6}	1.03×10^{-4}
^{32}S	16	4.17×10^{-4}	2.54×10^{-4}
^{36}S	16	9.87×10^{-8}	4.74×10^{-6}
^{40}Ar	18	0.00	8.53×10^{-6}
^{46}Ca	20	3.56×10^{-9}	2.81×10^{-6}
^{45}Sc	21	4.90×10^{-8}	9.16×10^{-7}
^{56}Fe	26	1.40×10^{-3}	1.66×10^{-4}
^{60}Fe	26	0.00	4.94×10^{-4}
^{59}Co	27	4.15×10^{-6}	1.04×10^{-4}
^{63}Ni	28	0.00	8.04×10^{-5}
^{64}Ni	28	8.96×10^{-7}	1.50×10^{-4}
^{63}Cu	29	7.35×10^{-7}	3.25×10^{-6}
^{65}Cu	29	3.38×10^{-7}	3.00×10^{-5}
^{64}Zn	30	1.26×10^{-6}	1.11×10^{-7}
^{69}Ga	31	4.84×10^{-8}	3.46×10^{-6}
^{70}Ge	32	5.29×10^{-8}	3.67×10^{-6}
^{75}As	33	1.52×10^{-8}	4.97×10^{-7}
^{76}Se	34	1.54×10^{-8}	1.31×10^{-6}
^{80}Se	34	9.06×10^{-8}	3.47×10^{-6}
^{79}Br	35	1.50×10^{-8}	1.34×10^{-7}
^{80}Kr	36	3.14×10^{-9}	2.05×10^{-8}
^{86}Kr	36	2.65×10^{-8}	2.90×10^{-6}
^{87}Rb	37	5.38×10^{-9}	1.59×10^{-6}
^{86}Sr	38	6.14×10^{-9}	1.89×10^{-7}
^{87}Sr	38	4.34×10^{-9}	3.22×10^{-8}
^{88}Sr	38	5.23×10^{-8}	1.61×10^{-6}
^{89}Y	39	1.31×10^{-8}	4.26×10^{-7}
^{90}Zr	40	1.63×10^{-8}	4.70×10^{-8}
^{96}Zr	40	9.47×10^{-10}	2.21×10^{-7}
^{138}Ba	56	1.42×10^{-8}	2.08×10^{-8}
^{139}La	57	1.99×10^{-9}	2.54×10^{-9}
^{208}Pb	82	1.21×10^{-8}	2.78×10^{-8}

minima observed in Fig. 9 correspond to the position of the He-burning shell while the following local maxima are determined by the interplay between the low mixing efficiency during the He-flash and the quiescent He-burning after the RLOF episode. This sequence of events is well illustrated in Fig. 7. The same effects define less expressed saw-tooth-like distribution of other isotopes.

Alpha-captures on ^{22}Ne produce ^{25}Mg, which acts as a strong neutron poison due to its large neutron capture cross-section (see e.g. Massimi et al. 2017); hence ^{26}Mg is efficiently produced via the ^{25}Mg(n,γ)^{26}Mg reaction.

Fig. 9 also reveals that α-isotopes are produced at a very high level. During the first He-flash episodes, when the maximum attained temperature is not very large, mainly, ^{16}O, ^{20}Ne, and ^{24}Mg are produced. After the 42th He-flash also ^{28}Si is efficiently

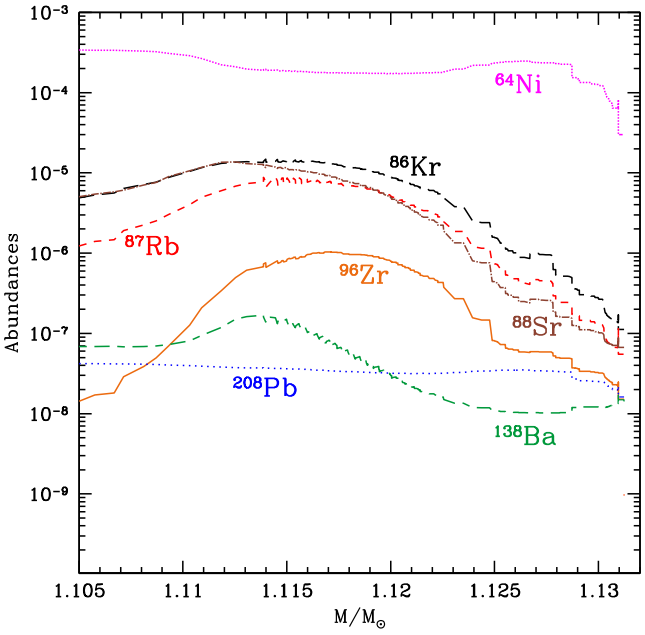

Figure 10. Abundances of selected heavy isotopes, tracing the *s*-process nucleosynthesis occurring on the accreting WD during SF accretion regime. Fine-dotted line: ^{64}Ni; long-dashed line: ^{86}Kr; short-dashed line: ^{87}Rb; dot–dashed line: ^{88}Sr solid line: ^{96}Zr; long–short dashed line: ^{138}Ba; dotted line: ^{208}Pb.

produced. Fig. 9 also shows that ^{32}S is partially destroyed (factor $\sim$ 2) pulse by pulse mainly via the ^{32}S(n,γ)^{33}S reaction, while it is produced after the 85th flash via α-capture on ^{28}Si. As a matter of fact, the maximum temperature attained during the SF accretion regime is not so high to allow the sizable production of heavier α-isotopes. The production of ^{24}Mg plays a pivotal role in determining the *n*-capture nucleosynthesis because, like ^{25}Mg, it acts as a strong poison.

In Fig. 10, we report the chemical profiles of some heavy isotopes, representative of the nucleosynthesis of *n*-rich isotopes occurring in the He-rich buffer during the flash episodes. We plot ^{88}Sr, ^{138}Ba, and ^{208}Pb as tracers of the three peaks of the *s*-process. While ^{88}Sr is, on average, overproduced by a factor $\approx$100, the other two isotopes show mild overabundance with respect to their initial values. This is somewhat expected because neutrons are released at the He-burning shell via ^{22}Ne(α, *n*)^{25}Mg and are locally captured, while the new synthesized heavy isotopes are moved outwards by convection, thus avoiding their local pile-up. As a consequence, abundance of elements beyond the first neutron magic number ($N = 50$) is only marginally enhanced (by less than a factor 5).

In Fig. 10, we also report the profiles of some *n*-rich isotopes, whose production in AGB stars is normally ascribed to the ^{22}Ne(α, *n*)^{25}Mg reaction (e.g. ^{86}Kr, ^{87}Rb, and ^{96}Zr). For these isotopes, the overproduction factors are even larger than for isotopes belonging to the three peaks of the *s*-process (up to a factor $\sim$ 1000 for ^{96}Zr). Fig. 10 also discloses that for M$\gtrsim$1.115 M$_{\odot}$, abundances of all isotopes with A>90 start to decrease. Such an occurrence corresponds to the large production of neutron poisons, in particular ^{24}Mg (see Fig. 9), which, as a matter of fact, largely reduces the total neutron exposure available for *n*-capture nucleosynthesis. Isotopes with A<90 exhibit the same behaviour, even if it occurs at larger masses (i.e. at later evolutionary time). In fact, the abundance of these isotopes is determined mainly by the peak neutron density

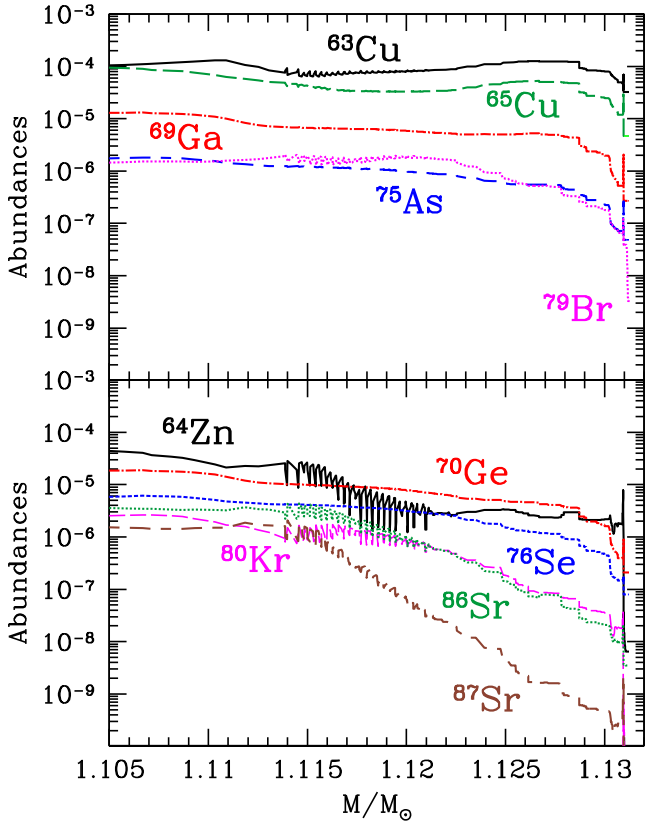

Figure 11. As in Fig. 10, but for isotopes normally ascribed to the *weak* *s*-process (upper panel) and for *s*-only isotopes (lower panel). Upper panel: solid line: ^{63}Cu; long-dashed line: ^{65}Cu; dot–dashed line: ^{69}Ga; long–short dashed line: ^{75}As; dotted line: ^{79}Br. Lower panel: solid line: ^{64}Zn; dot–dashed line: ^{70}Ge; short-dashed line: ^{76}Se; long-dashed: ^{80}Kr; dotted line: ^{86}Sr; long–short dashed:^{87}Sr.

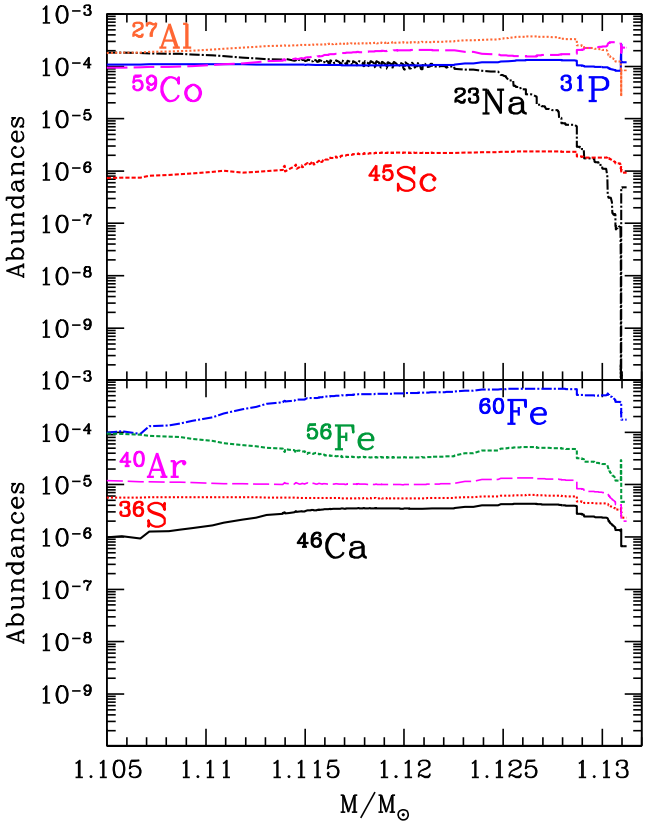

Figure 12. As in Fig. 10, but for light *n*-rich isotopes (lower panel) and light mono-isotopic elements (upper panel). Upper panel: dot–dashed line: ^{23}Na; dotted line: ^{27}Al; solid line: ^{31}P; short-dashed line: ^{45}Sc; long dashed line: ^{59}Co. Lower panel: dotted line: ^{36}S; long dashed line: ^{40}Ar; short-dashed line: ^{56}Fe; dot–dashed line : ^{60}Fe.

and, hence, is less dependent on the neutron poison abundances. The reduced efficiency in producing these latter isotopes has to be ascribed to the fact that, as matter is accreted, the time duration of the He-flash becomes shorter and, hence, also the duration of the peak phase of $n_n^{\max}$ becomes shorter (see Fig. 8). Neutron-rich isotopes with A<65 continue to be synthesized at a very high level, at least up to when a substantial neutron flux is available. For instance, ^{64}Ni is overproduced by a factor ∼300 up to the 76th flash episode, corresponding to $M_{\rm WD} = 1.1278$ M$_\odot$. Later on, neutron flux is reduced due to the efficient production of ^{28}Si and, less, of ^{32}S (see Fig. 9). These α-isotopes act as a strong neutron-poison, as their *n*-capture cross-section in the range (5–8) × 10^8 K is comparable with that of ^{24}Mg.

In the upper panel of Fig. 11, we report the profiles of isotopes normally ascribed to the *weak* *s*-process, demonstrating that the accretor in the S102 + 030 system strongly overproduces *weak-s* elements. Among the others, ^{63}Cu exhibits a large overabundance due also to the important radiogenic contribution from ^{63}Ni. In the lower panel of Fig. 11, we report the profiles of some *s*-only isotopes whose production is shielded by any contribution from the *r*-process by their stable isobars (e.g. the couples ^{64}Zn–^{64}Ni, ^{80}Kr–^{80}Se, and ^{87}Sr–^{87}Rb). For all these isotopes we obtain very large overproduction factor at least up to when the increasing production of the ^{24}Mg poison as well as the reduction of the neutron exposure make their synthesis less efficient (see the decrease in the profiles starting at $M_{\rm WD}$∼1.115 M$_\odot$).

As displayed in the lower panel of Fig. 12, there are other neutron-rich isotopes whose production, contrarily to main *s*-process elements, continuously grows flash after flash. This is the case, for instance, of unstable isotope ^{60}Fe, whose half-life is ∼1.5 × 10^6 yr. This isotope is of great interest for the astrophysical community, because it has been proved to be alive in the early Solar system (Mostefaoui, Lugmair & Hoppe 2005; Tang & Dauphas 2012). The accreting WD in the S102 + 030 system produces a large amount of ^{60}Fe, its abundance increasing up to 10^{-3}. The same behaviour is found for other *n*-rich isotopes, as ^{36}S, ^{40}Ar, and ^{46}Ca. As a matter of fact, when neutron poisons are largely overabundant and/or neutron exposures are very low, only these isotopes show a significant production, in spite of the extremely large neutron densities attained.

At odds with the *n*-rich heavy elements nucleosynthesis discussed above, the evolution of light elements abundance, as ^{19}F and ^{23}Na, holds few surprises (see upper panel in Fig. 12). Fluorine is heavily destroyed, due to its high volatility in hot stellar interiors. Sodium is destroyed at high temperatures via the ^{23}Na(α,p)^{26}Mg reaction, whose cross-section behaves similar to that of the ^{24}Mg(α, γ)^{28}Si (see the decrease of ^{23}Na abundance in the upper panel of Fig. 12). Aluminum shows an almost zero production. On the contrary, phosphorus and scandium, which are mildly produced by standard *s*-process, exhibit a moderate overproduction by a factor ∼10–20. Finally, cobalt shows a flat overproduction by a factor ∼15–20 all over the accreted layers. This is due to its vicinity to the main seeds for *n*-captures process, i.e. ^{56}Fe nuclei, which are almost uniformly

destroyed over the whole time-span of SF accretion regime (see lower panel in Fig. 12).

The chemical composition of the matter ejected pulse by pulse depends not only on the nucleosynthesis occurring during each He-flash, but also on the mass extension of the flash-driven convective shell and on the amount of mass ejected during the RLOF. In fact, heavy elements produced during the flash in the He-burning shell are dredged-up by convection. If the outermost zones unstable to convection are eroded by the RLOF-triggered mass-loss, the ejected matter will be enriched in heavy elements. Of course, the stronger the He-flash, the more extended the convective shell, the larger the mass lost during the RLOF and, hence, larger the heavy elements abundance in the ejected matter. In particular the abundance of the *j*-isotope in the ejected matter can be expressed as:

$$X_j^{\rm ej} = \frac{\Delta M_1}{\Delta M_{\rm lost}} X_j^{cv} + \frac{\Delta M_2}{\Delta M_{\rm lost}} X_j^{\rm acc}\,, \tag{4}$$

where $X_j^{\rm cv}$ and $X_j^{\rm acc}$ represent abundance of the *j*-isotope in the zone unstable for convection and that in the accreted matter, respectively. $\Delta M_{\rm lost} = M^1_{\rm WD} - M^2_{\rm WD}$ is the amount of mass lost during the RLOF and $M^1_{\rm WD}$, $M^2_{\rm WD}$ are the WD mass at the onset and at the end of the RLOF episode, respectively.

By defining $M^{\rm cv}_{\rm max}$ as the larger mass coordinate attained by convection during the flash episode, it comes out that $\Delta M_1 = \max(0, M^{cv}_{\rm max} - M^2_{\rm WD})$ and $\Delta M_2 = \min(\Delta M_{\rm lost}, M^1_{\rm WD} - M^{\rm cv}_{\rm max})$. Equation (4) clearly suggests that the heavy elements abundance in the ejected matter is expected to be lower than that in the surface layer of the WD after each flash. As pulse by pulse the convective unstable zone approaches the WD surface, the ratio $X_j^{\rm ej}/X_j^{\rm cv}$ increases up to its maximum value, i.e. 1.

To analyse the heavy elements abundance in the ejected matter we use the *elemental enhancement factor* defined as

$$\Psi = \frac{N(el)_{\rm ej}}{N(el)_{\rm acc}} \tag{5}$$

where $N(el)_{\rm ej}$ and $N(el)_{\rm acc}$ are the number abundances of a given element in the ejected matter and in the accreted matter, respectively, and are defined as

$$N(el) = \sum_i \frac{X_i}{A_i} \tag{6}$$

the summation being extended to all the isotopes with atomic number $Z_{\rm el}$. By adopting the definition of $X_j^{\rm ej}$ in equation (4), the elemental enhancement factor can be written as

$$\Psi = \Psi_{\rm cv}\frac{\Delta M_1}{\Delta M_{\rm lost}} + \frac{\Delta M_2}{\Delta M_{\rm lost}}, \tag{7}$$

where $\Psi_{\rm cv}$ is the elemental enhancement factor in the zone unstable for convection.

As a matter of fact, we found that during the RLOF episodes triggered by the first four strong He-flashes the ejected matter is not enriched at all in heavy elements. In fact, the energy released by the flash is not very large so that the flash-driven convective zone remains confined in the innermost part of the He-rich layers and the mass lost during the RLOF episode is very low. Moreover, the external border of the flash-driven convective shell attains the WD surface during the 42th flash, so that from this epoch up to the last He-flash $\Psi = \Psi_{\rm cv}$. In Fig. 13, we plot (top to bottom) the Ψ value for the ejected matter during the 38th, 67th, 76th, and the 87th RLOF episodes; in the bottom panel we report the total elemental enhancement factor for the entire mass ejected during the SF accretion regime, equal to $M^{\rm tot}_{\rm ej} = 5.012 \times 10^{-2}$ M$_\odot$. To evaluate such a quantity we assume that the matter ejected at each RLOF episode is fully mixed.[5] Fig. 13 shows that ejected matter is mainly enriched in α-elements (up to ^{28}Si), by a factor 10–100 and in light-*s* elements (Sr, Y, Zr). In the last column of Table 4, we list the abundances of selected isotopes in the matter ejected during the SF accretion regime ($X_{\rm ej}$).

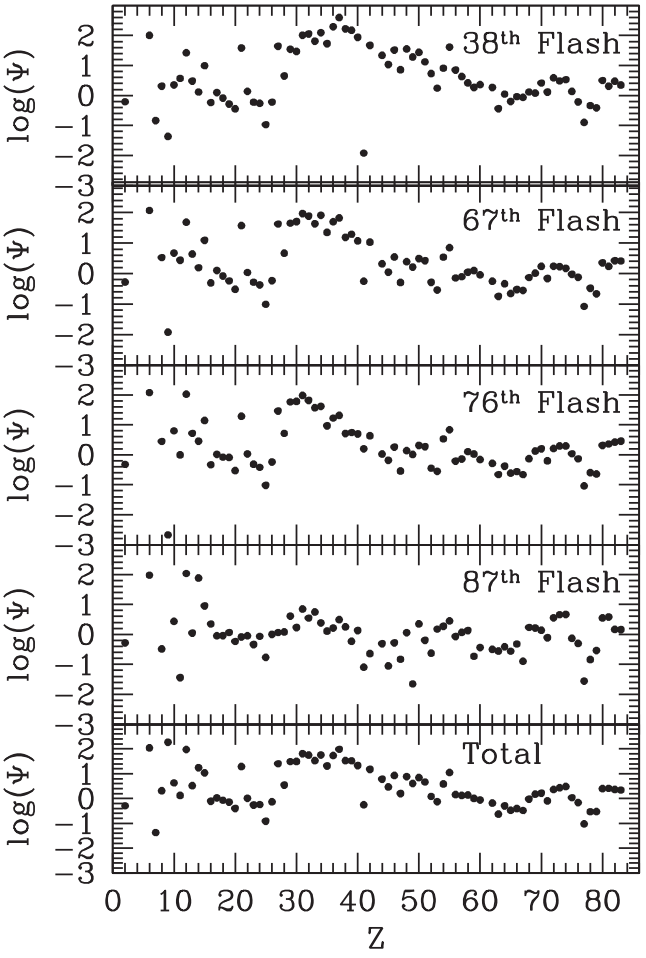

Figure 13. Elemental enhancement factor Ψ in the matter ejected during the 38th, 67th, 76th, and 87th RLOF episodes, as labelled. The bottom panel shows the same quantity for the total mass ejected during the SF accretion regime.

Kupfer et al. (2013) discovered an excess of Mg in the spectrum of a long-period (52.96 ± 0.40 min) AM CVn-type system. The origin of excess should be associated with accretor, since donor (respectively disc) matter does not have excess of Mg. ^{24}Mg is efficiently produced when the temperature in the He-burning layer increases above $\sim 2.5 \times 10^8$ K. In the S102 + 030 system the outbursts in which ^{24}Mg may be produced occur at $P_{\rm orb}$ below 10 min (see e.g. Fig. 3 or 5), within about 1 Myr after the formation of the system. Evolution to $P_{\rm orb} \approx 53$ min takes about 1.5 Gyr. In this time, about 0.05 M$_\odot$ of matter non-enriched by magnesium is transferred to the accretor. Outer layers of WD may become enriched in ^{24}Mg if, for instance, accreted matter mixes with underlying layers due to rotation. We may expect that a similar

[5]This assumption is justified by the circumstance that most matter is lost in the last ∼10 strong flashes, during which convective zone extends to the surface of accretor.

process may occur in the AM CVn stars with He-star donors, since accretors in them also experience outbursts with high enough temperature (Brooks et al. 2015) and these systems also may evolve to long orbital periods (Yungelson 2008). But a more detailed study of this issue is beyond the scope of this paper.

6 DISCUSSION AND CONCLUSION

This study is devoted to the investigation of physical and chemical evolution of extreme IDD AM CVn stars with both massive CO WD accretors and He WD donors at the very early stage of their evolution (about first 60 000 yr after formation in this case), when they have orbital periods below ~ 10 min. As in our previous study (Paper II) we model the donor as cool degenerate object obeying the Zapolsky & Salpeter (1969) M–R relation and adopt a time-dependent mass accretion rate as determined by angular momentum losses via emission of GWs. We also assume that possible RLOF by the accreting WD triggers the loss of matter from the system with specific angular momentum of the accretor. In these systems the temperature attained in the He-burning shell during recurrent flash episodes is so large that a full nuclear network is necessary in order to correctly evaluate the energy contribution from α-capture as well as from *n*-capture processes.

After the initial flash, that follows accumulation of the first layer of He susceptible to thermonuclear instability, as the mass transfer rate from the donor is continuously decreasing, massive IDDs enter steady accretion regime. From this epoch on, the evolution of the S102 + 030 system occurs exactly as in systems with degenerate He WD of lower mass. In particular, we confirm our previous finding that accretors in IDDs end their evolution as CO WDs capped by a massive He-buffer, without developing the 'last' very strong dynamical He-flash able to produce an SN .Ia (Bildsten et al. 2007). It has to be noticed that, according to Brooks et al. (2015), also AM CVn stars of the 'He-star family' never experience dynamical 'last' He-flash.

At variance with systems considered in Paper II, we found that in IDD systems with massive donors the temperature in the He-shell exceeds 3×10^8 K already during the MF accretion phase. As a consequence, ^{22}Ne$(\alpha, n)^{25}$Mg reactions are fully ignited and *n*-capture nucleosynthesis can occur. We demonstrate that (see Fig. 5) the inclusion of the energy coming from *n*-capture processes largely affects the retention efficiency during the SF accretion phase, determining a final CO core less massive as compared to the case when incomplete nuclear network is adopted in the computation. However, our results also show that the evolutionary outcome of massive AM CVn stars does not depend on the inclusion or not of *n*-capture processes in the adopted nuclear network.

The detailed computation of the evolution of the S102 + 030 system shows that during the SF accretion regime maximum temperature attained during He-flashes progressively increases from $\sim 3 \times 10^8$ to $\sim 7.6 \times 10^8$ K, corresponding to maximum neutron densities of 10^{11} cm^{-3} (typical of *s*-process nucleosynthesis in intermediate-mass AGB stars) and $\sim 3 \times 10^{16}$ cm^{-3} (typical of *i*-process nucleosynthesis), respectively. Even if the total neutron exposure largely increases pulse by pulse, the neutron flux available for the nucleosynthesis of *n*-rich heavy isotopes largely reduces after about 40 He-flash episodes. In fact, α-isotopes produced by He-burning (mainly ^{24}Mg, ^{28}Si) and their *n*-capture daughters nuclei act as strong neutron-poisons due to their very large abundances. As a consequence, we found that during the first He-flash episodes elements belonging to all the three *s*-process peaks are overproduced by a large factor. Then, pulse by pulse, the enhancement factor Ψ of elements belonging to the third and subsequently also to the second *s*-process peaks rapidly decreases to one.

In summary, the nucleosynthesis in massive AM CVn stars like the system S102 + 030 is expected to show the typical pattern of the *weak* component of *s*-process, superimposed to a tail extending to heavier elements (resulting from an efficient ^{22}Ne burning in a hot convective environment), with local peaks corresponding to very *n*-rich isotopes, tracers of the activation of a very high-temperature *i*-process. To our knowledge, this is the first paper dealing with an *i*-process related to the ^{22}Ne + α source.

It is interesting to note that the nucleosynthesis depends mainly on the metallicity of the He WD progenitor. In fact, the latter determines the amount of ^{14}N in the accreted matter and, hence, of neutrons delivered via ^{22}Ne$(\alpha, n)^{25}$Mg reactions. As a consequence, AM CVn stars like S102 + 030 with low metallicity stellar progenitors are expected to scarcely produce also elements belonging to the first *s*-peak, while those with large metallicity ($Z \geq 2Z_{\odot}$) could produce efficiently also heavy-*s* elements (Ba, La, Nd, Sm).

The S102 + 030 system ejected into the interstellar medium $\approx 5.2 \times 10^{-2}$ M$_{\odot}$ with the same chemical composition of the accreted matter during the evolution in the RG-burning regime and $\approx 5.1 \times 10^{-2}$ M$_{\odot}$ of matter with enhanced abundance of α- and *n*-rich isotopes. (see Table 4 and Fig. 13).

AM CVn stars similar to the S102 + 030 system are expected to be very rare, having formation rate of $\sim 10^{-6} \div 10^{-5}$ yr^{-1} (Nelemans et al. 2001). As a consequence, their contribution to the Galactic chemical evolution is, most probably, insignificant.

Though many instances of stellar evolution involving *i*-process have been investigated already, for sure they are not exhaustive of the plethora of minor nucleosynthesis events at work in stellar interiors. Whenever sufficient amounts of ^{13}C or ^{22}Ne are stored in a stellar layer, in fact, a new type of nucleosynthesis may develop. The efficiency of these processes obviously depends on the temperature to which the material is exposed, on environment conditions (radiative/convective), and on the time-scale of the evolutionary phase. Systems similar to S102 + 30 are an example of such 'peculiar' nucleosynthesis sources.

ACKNOWLEDGEMENTS

We acknowledge the referee for insightful comments. We are indebted to G. Ramsey for providing us mass-transfer rates based on Bildsten et al. (2006) mass–radius relation. LRY ackowledges hospitality and support of Rome and Teramo observatories and Max Planck Institute for Astrophysics (Garching) where a part of this study was accomplished.

REFERENCES

Bildsten L., Townsley D. M., Deloye C. J., Nelemans G., 2006, ApJ, 640, 466
Bildsten L., Shen K. J., Weinberg N. N., Nelemans G., 2007, ApJ, 662, L95
Brooks J., Bildsten L., Marchant P., Paxton B., 2015, ApJ, 807, 74
Burbidge E. M., Burbidge G. R., Fowler W. A., Hoyle F., 1957, Rev. Mod. Phys., 29, 547
Chieffi A., Limongi M., 2013, ApJ, 764, 21
Côté B., Denissenkov P., Herwig F., Ruiter A. J., Ritter C., Pignatari M., Belczynski K., 2018, ApJ, 854, 105
Cowan J. J., Rose W. K., 1977, ApJ, 212, 149
Cristallo S. et al., 2011, ApJS, 197, 17
Cristallo S., Straniero O., Piersanti L., Gobrecht D., 2015, ApJS, 219, 40
Cristallo S., Karinkuzhi D., Goswami A., Piersanti L., Gobrecht D., 2016, ApJ, 833, 181

Denissenkov P. A., Herwig F., Battino U., Ritter C., Pignatari M., Jones S., Paxton B., 2017, ApJ, 834, L10
Farouqi K., Kratz K.-L., Mashonkina L. I., Pfeiffer B., Cowan J. J., Thielemann F.-K., Truran J. W., 2009, ApJ, 694, L49
Fuller J., Lai D., 2012, ApJ, 756, L17
Gallino R., Arlandini C., Busso M., Lugaro M., Travaglio C., Straniero O., Chieffi A., Limongi M., 1998, ApJ, 497, 388
Iben I., Jr., Tutukov A. V., Fedorova A. V., 1998, ApJ, 503, 344
Kasen D., Metzger B., Barnes J., Quataert E., Ramirez-Ruiz E., 2017, Nature, 551, 80
Kupfer T., Groot P. J., Levitan D., Steeghs D., Marsh T. R., Rutten R. G. M., Nelemans G., 2013, MNRAS, 432, 2048
Lauffer G. R., Romero A. D., Kepler S. O., 2018, MNRAS, 480, 1547
Marsh T. R., Nelemans G., Steeghs D., 2004, MNRAS, 350, 113
Massimi C. et al., 2017, Phys. Lett., 768, 1
Mostefaoui S., Lugmair G. W., Hoppe P., 2005, ApJ, 625, 271
Nelemans G., 2005, in Hameury J.-M., Lasota J.-P., eds, ASP Conf. Ser., Vol. 330, The Astrophysics of Cataclysmic Variables and Related Objects. Astron. Soc. Pac., San Francisco, p. 27
Nelemans G., 2009, Class. Quantum Gravity, 26, 094030
Nelemans G., Portegies Zwart S. F., Verbunt F., Yungelson L. R., 2001, A&A, 368, 939
Nishimura N., Sawai H., Takiwaki T., Yamada S., Thielemann F.-K., 2017, ApJ, 836, L21
Nomoto K., 1982, ApJ, 253, 798
Panei J. A., Althaus L. G., Chen X., Han Z., 2007, MNRAS, 382, 779
Piersanti L., Tornambé A., Yungelson L. R., 2014, MNRAS, 445, 3239
Piersanti L., Yungelson L. R., Tornambé A., 2015, MNRAS, 452, 2897
Prantzos N., Hashimoto M., Nomoto K., 1990, A&A, 234, 211
Ramsay G. et al., 2018, A&A, 620, A141
Savonije G. J., de Kool M., van den Heuvel E. P. J., 1986, A&A, 155, 51
Shen K. J., 2015, ApJ, 805, L6
Solheim J., 2010, PASP, 122, 1133
Straniero O., Gallino R., Cristallo S., 2006, Nucl. Phys., 777, 311
Tang H., Dauphas N., 2012, Earth Planet. Sci. Lett., 359, 248
Tutukov A., Yungelson L., 1996, MNRAS, 280, 1035
Tutukov A. V., Fedorova A. V., Ergma E. V., Yungelson L. R., 1985, Sov. Astron. Lett., 11, 52
Verbunt F., Rappaport S., 1988, ApJ, 332, 193
Wu C., Wang B., Liu D., Han Z., 2017, A&A, 604, A31
Yungelson L. R., 2008, Astron. Lett., 34, 620
Zapolsky H. S., Salpeter E. E., 1969, ApJ, 158, 809

This paper has been typeset from a TEX/LATEX file prepared by the author.